Chemical Science

ROYAL SOCIETY OF CHEMISTRY

EDGE ARTICLE

View Article Online
View Journal

Cite this: DOI: 10.1039/d6sc00647g

All publication charges for this article have been paid for by the Royal Society of Chemistry

The underlying synergistic mechanism of co-solvents to fabricate high-quality $FAPbI_3$ perovskite films

Zezhuan Jiang,[a] Xiaofeng He,[ab] Cunyun Xu,[a] Xiaoyun Wan,[c] Haimao Zhu,[a] Jiancheng You,[a] Zhongjun Dai,[a] Wenqi Zeng,[a] Ping Li,*[d] Jin Ye*[a] and Qunliang Song*[a]

The quality of perovskite layers is a critical factor in determining the performance of perovskite solar cells (PSCs). α-$FAPbI_3$ is a promising absorber material, but fabricating high quality metastable α-$FAPbI_3$ thin films remains challenging due to poor control over intermediate phases during deposition. Although co-solvent strategies have been identified as an effective method to control these intermediate phases, the underlying mechanism is not fully understood. In this study, we systematically investigate the synergistic effects of DMSO and NMP co-solvents on perovskite mesophase formation, combining theoretical and experimental insights into intermediate phase control and α-$FAPbI_3$ crystallization. Using *in situ* photoluminescence (PL) monitoring during spin-coating, together with density functional theory (DFT) calculations and Fourier-transform infrared (FTIR) spectroscopy, we reveal how solvent competition modulates intermediate complex formation and evolution. The synergistic effect of these solvents was finally disclosed, which effectively governs the formation and evolution of the intermediate phases. The optimized co-solvent system promotes the transformation of intermediates into α-$FAPbI_3$ at lower thermodynamic transition temperatures, yielding high phase purity and low defect density. As a result, PSCs fabricated using this approach achieved a power conversion efficiency (PCE) of 22.80% with improved stability. The insights gained from this work provide a rational framework for solvent selection in the fabrication of high-quality perovskite films for advanced photovoltaics.

Received 23rd January 2026
Accepted 26th March 2026

DOI: 10.1039/d6sc00647g

rsc.li/chemical-science

1. Introduction

Hybrid organic–inorganic metal halide perovskite solar cells (PSCs) have now achieved a power conversion efficiency (PCE) of up to 27%,[1] owing to the excellent optoelectronic properties of perovskite materials, such as tunable bandgaps, high absorption coefficients, and long carrier diffusion lengths.[2–4] Among them, formamidinium lead tri-iodide ($FAPbI_3$) has attracted widespread attention due to its near-ideal bandgap and thermal stability. $FAPbI_3$ crystallizes in two main phases: the photoactive black α-phase and the non-perovskite yellow δ-phase. The α-phase has been extensively used as the absorber in high-efficiency PSCs.[5–8] Unfortunately, controlling the nucleation and crystal growth of α-$FAPbI_3$ is challenging,[9,10] as the δ-phase is thermodynamically favored under ambient conditions. A common approach to stabilize α-$FAPbI_3$ involves incorporating methylammonium chloride (MACl and Cs) into precursor solution, a widely proven effective method for increasing the performance of polycrystalline perovskite films.[11–13] Some other strategies have also been proved to be very effective to obtain high quality α-$FAPbI_3$ films, such as annealing conditions,[14] humidity control,[15] and interface engineering,[16–19] which have also served as important strategies for achieving improved film quality and device performance.

Another effective approach to achieve high quality α-phase $FAPbI_3$ films is to regulate perovskite intermediate phases (*e.g.* δ-phase or solvent adducts) through solvent engineering.[10,20–22] The most commonly used solvents for intermediate-phase control include dimethyl sulfoxide (DMSO) and *N*-methyl-2-pyrrolidone (NMP).[23] For example, Yang *et al.*[20] replaced DMSO with NMP to form a stable intermediate adduct that converted into a uniform, pinhole-free $FAPbI_3$ film upon thermal annealing. Similarly, Bu *et al.*[10] regulated the ratio of *N*,*N*-dimethylformamide (DMF), DMSO, and NMP in the perovskite precursor solvent to form PbI_2–solvent adducts that reduced the δ-to-α phase transition barrier. Huang *et al.*[21] demonstrated that hydrogen-bond-favorable intermediates,

[a]*Institute for Clean Energy and Advanced Materials, School of Materials and Energy, Southwest University, Chongqing Key Laboratory for Advanced Materials and Technologies of Clean Energy, Chongqing 400715, P. R. China*

[b]*Yibin Academy of Southwest University, Yibin 644000, China*

[c]*School of Physics and Electronic Science, East China Normal University, 500 Dongchuan Road, Shanghai 200241, China*

[d]*School of Physics and Electronic Science, Zunyi Normal University, Zunyi 563006, P. R. China*

such as (FA···NMP)PbI_3, facilitate defect-free α-$FAPbI_3$ formation. Nevertheless, a fundamental trade-off exists: strongly coordinating solvents (*e.g.*, DMSO) stabilize the δ-phase and passivate activate Pb–I bonds, but slow solvent removal hinders rapid transition to the α-phase.[24–26] In contrast, relatively weakly coordinating solvents such as NMP can significantly reduce δ-phase formation and enable low-temperature phase transitions, but may lead to smaller grain sizes in the final perovskite films.[27,28] Although DMSO/NMP co-solvent systems have been shown to improve film quality,[29–31] a more in-depth understanding of how mixed solvents influence $FAPbI_3$ nucleation films is still lacking. Experimentally, optimizing the DMSO/NMP ratio is ongoing to identify an optimal solvent recipe.

In this work, we disclosed the synergistic effects of DMSO/NMP co-solvents theoretically and experimentally. The high-quality $FAPbI_3$ perovskite films fabricated by using DMSO/NMP mixed solvents were also demonstrated. Our results demonstrate that 1 : 1 molar ratio of NMP : DMSO optimally controls intermediate phase formation, resulting in high-quality $Cs_{0.04}FA_{0.96}PbI_3$ films with large grain sizes, low defect densities, and negligible cracks or pores. The resulting solar cells achieve a PCE of 22.80%, highlighting the efficacy of this co-solvent strategy in advancing perovskite photovoltaics.

2. Results and discussion

In this work, we focus on widely used oxygen-containing Lewis base solvents (DMSO and NMP), which feature structures similar to oxygen-containing double bonds. The commonly used MACl additive and the incorporation of Cs are referenced as strategies to stabilize the phase structure and reduce the formation energy of $FAPbI_3$.[11–13] To investigate nucleation and crystal growth, we employed the $Cs_{0.04}FA_{0.96}PbI_3$ perovskite composition and corresponding devices. Since film morphology is influenced by intermediate complexes formed through coordination bonds in the precursor solution, we first investigated solute–solvent interactions. We combined density functional theory (DFT), electrostatic potential (ESP) mapping and gas-phase binding-energy calculations ($DMol^3$, PBE/DNP) with FTIR to study the coordination between DMSO/NMP and the perovskite precursors (PbI_2 and FAI). As illustrated in Fig. 1a–d, the oxygen atoms in DMSO and NMP (the molecular structures of DMSO and NMP are shown in Fig. S1a and b), typically represented as S=O and C=O groups, exhibit negative ESP values, indicating nucleophilic sites that coordinate with Pb^{2+} (Fig. 1a and b).

Notably, the negative potential around DMSO's oxygen is more pronounced, suggesting stronger coordination than NMP. The outer surface of PbI_2 lies in the positive potential region (Fig. 1c), facilitating interactions with the negatively charged solvent oxygen atoms. In contrast, the NH_2–H group of FAI presents a positive potential hotspot (Fig. 1d), enabling only weak hydrogen bonding. Consequently, PbI_2 preferentially interacts with DMSO and NMP, while FAI plays a minor role.[10] FTIR spectra (Fig. 1e–i) revealed redshifted S=O and C=O stretching vibrations (1043 cm^{-1} for S=O in DMSO, Fig. 1e, 1671 cm^{-1} for C=O in NMP)[32] upon PbI_2 coordination, confirming adduct formation. When PbI_2 was combined with DMSO or NMP to form DMSO·PbI_2 and NMP·PbI_2 complexes, the S=O and C=O stretching vibration peaks shifted to lower wavenumbers—988 cm^{-1} (Fig. 1f) and 1620 cm^{-1} (Fig. 1g), respectively. When the DMSO content is increased, the smaller incremental shift of the S=O band is consistent with the presence of DMSO-rich, higher-coordination PbI_2 adducts in solution, potentially including PbI_2·2DMSO-like species. The larger shift for DMSO indicates stronger binding. As shown in Fig. 1h, when a 1 : 1 molar ratio of DMSO and NMP was added to PbI_2, the stretching vibration peaks of S=O and C=O appeared around 1020 cm^{-1} and 1619 cm^{-1}, respectively. In the 1 : 1 DMSO : NMP mixture, competitive coordination modulates the proportions of DMSO·PbI_2 and NMP·PbI_2 complexes, regulating intermediate phase formation. Additionally, as shown in Fig. 1i, changes in the N–H bending vibration were observed in the FAI co-solvent complexes. These changes are consistent with the fact that FAI molecules form hydrogen bonds more readily with NMP than with DMSO, as also observed in Fig. S2.[21] To complement the ESP/FTIR analysis, we computed gas-phase binding energies ($DMol^3$, PBE/DNP) for PbI_2–solvent adducts:

$$E_{\text{bind}}^{\text{neutral}} = E(\text{PbI}_2 - \text{L}) - \{E(\text{PbI}_2) + E(\text{L})\},$$

and, for the NMP deprotonation pathway,

$$E_{\text{bind}}^{\text{H}^+\text{ref}} = E(\text{PbI}_2 - \text{NMP}) - \{E(\text{PbI}_2) + E(\text{NMP})\},$$

with 1 H $a = 27.2114$ eV. Numerical results are summarized in Table S1. A single DMSO binds exothermically to PbI_2 (−0.32 eV), while adding a second DMSO is endothermic in the gas phase (+0.88 eV overall; stepwise $\Delta E = +1.20$ eV relative to PbI_2–DMSO). NMP binding becomes favorable only when considering a deprotonation pathway (≈ −1.05 eV *versus* an H^+ reference; the H-atom reference would give an unphysically large −13.4 eV). These results confirm the stronger coordination of DMSO to PbI_2 and show that the addition of a second DMSO to an isolated gas-phase adduct is energetically unfavorable in the absence of dielectric stabilization. Consequently, any higher-coordination DMSO-rich species present in the precursor solution are expected to be stabilized by the surrounding polar solvation environment, rather than persisting as isolated complexes under such conditions. Full definitions and total energies are provided in Table S1.

To further quantify co-solvent interactions, density functional theory (DFT) calculations were carried out using $DMol^3$ (BIOVIA Materials Studio software suite) on various cluster structures formed by PbI_2 and oxygen-containing double-bonded Lewis base solvent molecules (DMSO and NMP). These cluster-level energetics are consistent with the monomer benchmark, which captures the dual role of DMSO: it is a stronger ligand, but over-coordination is penalized in the isolated gas-phase. This suggests that mixed DMSO/NMP environments can stabilize multinuclear aggregates without locking PbI_2 into a DMSO-rich, over-coordinated state (Table S1). For a single PbI_2 molecule with a small number of solvent molecules (*e.g.*, 1 NMP + 1 DMSO), the system typically forms a simple mononuclear complex in which Pb is coordinated by

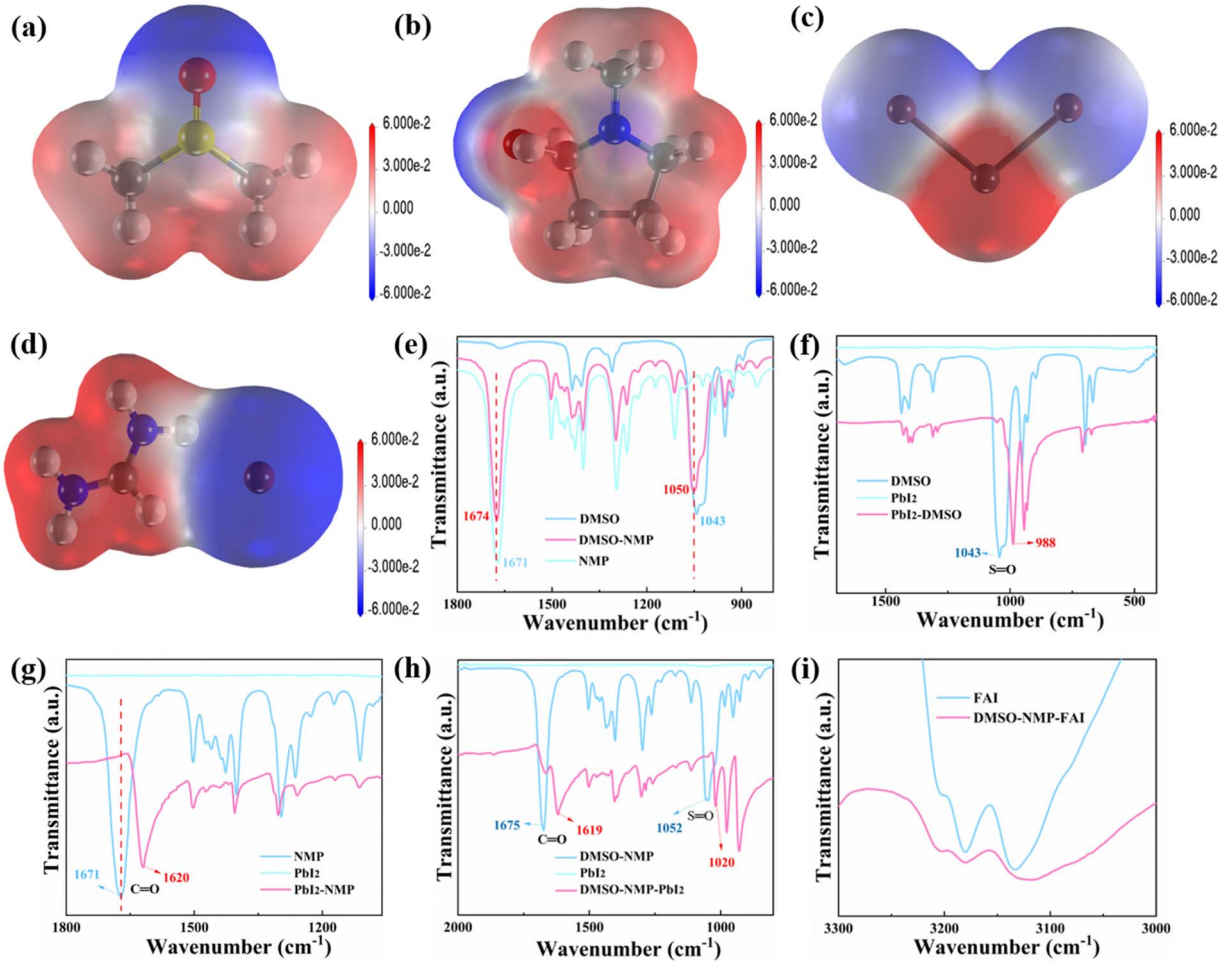

Fig. 1 Molecular structures with electrostatic potential (ESP) maps of (a) DMSO, (b) NMP, (c) PbI_2, and (d) FAI. FTIR spectra of (e) DMSO, NMP, and DMSO : NMP (1 : 1), (f) PbI_2 + DMSO, (g) PbI_2 + NMP, (h) PbI_2 + DMSO : NMP (1 : 1), and (i) FAI + DMSO : NMP (1 : 1).

halides (I^-) and solvent oxygen atoms (S═O or C═O) (Fig. S3a–d), with a coordination number of approximately 4–5. We further explored multinuclear clusters involving two PbI_2 units with DMSO and NMP. In these cases, Pb atoms may be interconnected *via* bridging iodides (μ_2-I) or may each be terminated by several iodides (terminal I). The polar oxygen atoms of DMSO and NMP can coordinate to the same or different Pb centers, thereby increasing the overall coordination number and enhancing electronic coupling. After geometric optimization, certain configurations exhibit Pb–I–Pb bond angles of 90–120° in bridging arrangements, with the solvent oxygen atoms tightly coordinated to Pb, effectively shielding the local positive charge of Pb^{2+} (Fig. S4a–c). Such aggregates exhibited lower total energies (by several eV) and reduced HOMO–LUMO gaps (~0.3–0.9 eV) (Table S2), indicating enhanced electronic coupling and stability. Even within the $2PbI_2$ + 1 DMSO + 1 NMP systems, a 1–2 eV difference was observed among different bridging and arrangement modes, reflecting the sensitivity of stability to steric effects and the specific bridging type (Fig. 2a–c). Within the same stoichiometry, the most stable configuration is ~2 eV lower in energy than the second most stable structure (Table S2); absolute total energies (*e.g.*, −67 615.28 Ha) are not compared across different stoichiometries that feature bridging iodides and coordinated solvent molecules, promoting charge delocalization and complex stability (Fig. 2b). The lowest-energy and most stable configurations typically correspond to the narrowest bandgap (~0.3 eV), suggesting significant electron cloud overlap and mixed ionic–covalent characteristics between Pb–I–ligand interactions. This effect may also explain the more pronounced shift in the stretching vibration peak of DMSO in the mixed solvent system compared with the single-solvent case (Fig. 1f and g). These findings suggest that the 1 : 1 DMSO : NMP ratio fosters optimal complexation, facilitating controlled nucleation and then high-quality perovskite films.

We then monitored the solution-to-film transition using *in situ* photoluminescence (PL) measurements during spin-coating. For $FAPbI_3$ precursors with MACl, anti-solvent dripping at ~20 s induced a transient PL peak, signifying brief α-phase formation followed by conversion to a non-emissive intermediate (Fig. 2d–f). This is owing to the fact that the anti-solvent plays a critical role in regulating perovskite crystallization by accelerating the solvent removal and initiating

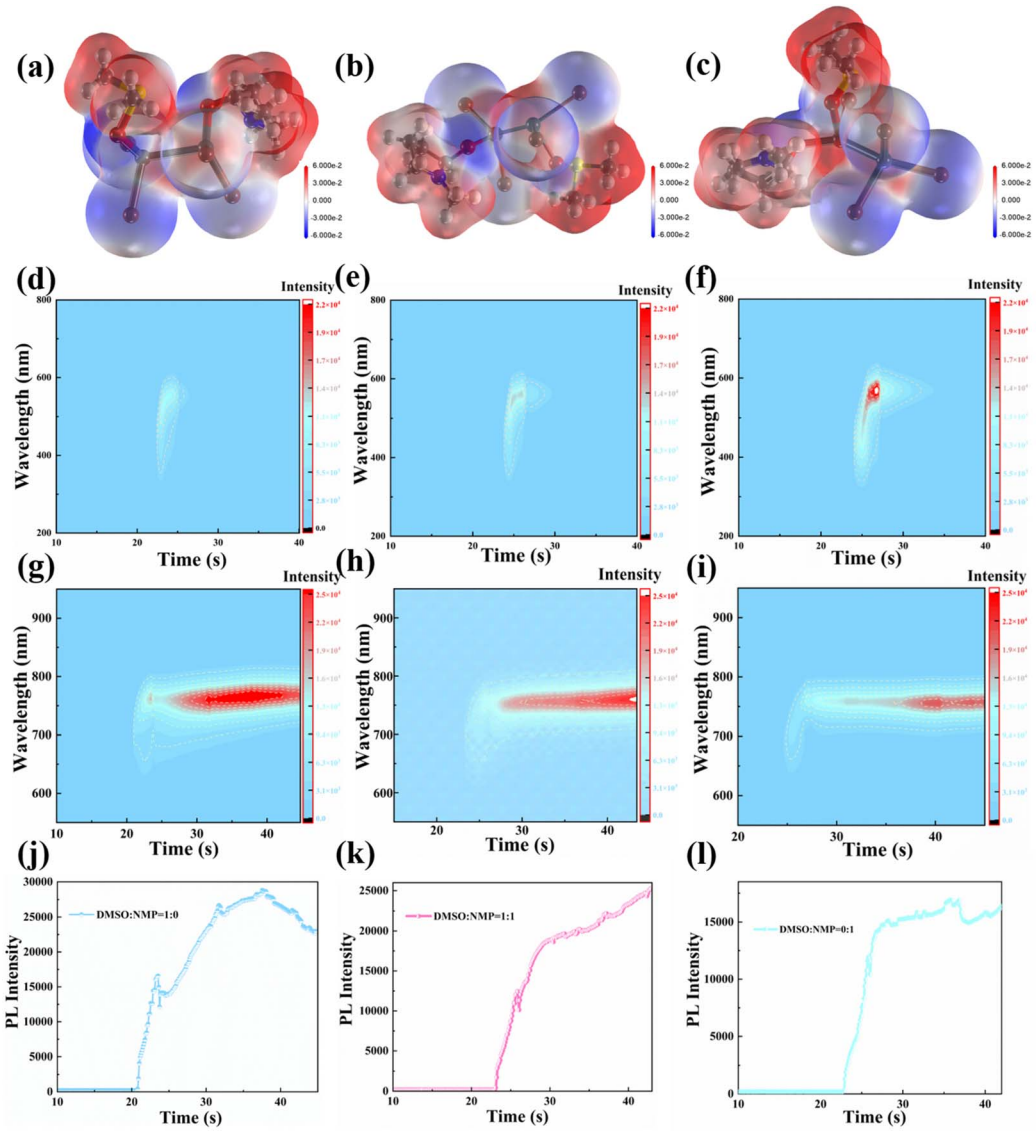

Fig. 2 Molecular structures with electrostatic potential (ESP) maps from DFT calculations: (a–c) cluster structures formed by PbI_2 and representative oxygen-containing Lewis base solvents with double bonds (DMSO and NMP). The *in situ* PL mapping during spin coating for different solvent components of $FAPbI_3$ precursors: (d) DMSO : NMP = 1 : 0, (e) DMSO : NMP = 1 : 1, (f) DMSO : NMP = 0 : 1 with MACl additives and for $Cs_{0.04}FA_{0.96}PbI_3$ precursors with different solvents: (g) DMSO : NMP = 1 : 0, (h) DMSO : NMP = 1 : 1, (i) DMSO : NMP = 0 : 1. The extracted maximum PL values of the $Cs_{0.04}FA_{0.96}PbI_3$ precursor perovskite film during spin coating of (j) DMSO, (k) DMSO : NMP, and (l) NMP from *in situ* PL mapping.

film formation.[33] After anti-solvent treatment, the film containing only the MACl additive did not transform into α-$FAPbI_3$, likely due to its relatively higher energy barrier. Instead, it preferentially formed δ-$FAPbI_3$ or a non-photoactive intermediate phase with lower formation energy. This explains why, in Fig. 2d–f, the PL signal appeared rapidly upon application of the solvent–evaporation droplet, and then gradually fade away. For comparison, *in situ* PL measurements of $FAPbI_3$ films without MACl showed no significant intensity variation, as illustrated in Fig. S5. Interestingly, in the NMP-based system (Fig. 2f), the PL intensity change was more pronounced. This may be attributed to the lower formation energy of the $FAI{\cdot}PbI_2{\cdot}$NMP intermediate, which facilitates its conversion into α-$FAPbI_3$.[10] In contrast, the $Cs_{0.04}FA_{0.96}PbI_3$ perovskite precursor exhibited sustained PL signals after anti-solvent application (Fig. 2g–i), indicating direct α-phase formation. The co-solvent system showed a gradual PL increase, reflecting regulated crystallization kinetics. This persistent intensity is likely due to incomplete removal of the main solvent, consistent with reports of DMSO residues in perovskite films.[34,35] This sustained PL behavior is attributed to the lower formation energy of the $FAI{\cdot}PbI_2{\cdot}$NMP complex. These observations are consistent with earlier reports indicating that NMP-based intermediates more readily convert into the photoactive perovskite phase.[10] These observations highlight the role of solvent composition in intermediate phase evolution and final film quality. The

maximum *in situ* PL intensities recorded during spin-coating for $Cs_{0.04}FA_{0.96}PbI_3$ precursors are shown in Fig. 2j–l. In the co-solvent system, the intermediate phase appears to be dominated by the combined solvent effect, which may increase solution viscosity,[36] enhance precursor stability, and is consistent with the results of our theoretical calculations. The co-solvent strategy therefore directly influences nucleation and crystallization dynamics.

X-ray diffraction (XRD) analysis of wet films (Fig. 3a, c and S6) confirmed that DMSO-rich precursors favored δ-$FAPbI_3$ (strong diffraction peak at 11.7°), while NMP-rich systems formed $FAI{\cdot}PbI_2{\cdot}NMP$ intermediates (two distinct peaks appeared in the 8–10° range).[10] In general, the DMSO-based samples exhibited a clear δ-phase of $FAPbI_3$, whereas less δ-phase was detected in the NMP-based samples. The 1 : 1 co-solvent suppressed δ-phase formation and promoted a balanced intermediate composition. After annealing, all films transformed into phase-pure α-$FAPbI_3$, with the 1 : 1 blend showing the highest crystallinity (Fig. 3b and d). As shown in Fig. 3a, samples prepared with other solvent ratios also exhibited clear signatures of such competitive intermediate-phase behavior. The synergistic intermediate phase obtained in this way enables reasonable control over solvent residues as well as crystallization nucleation and growth kinetics during annealing.

For $Cs_{0.04}FA_{0.96}PbI_3$ perovskite wet films, the introduction of Cs enabled the direct formation of a distinct α-$FAPbI_3$ phase immediately after spin-coating (Fig. S5). This explains why the $Cs_{0.04}FA_{0.96}PbI_3$ wet film maintained a strong PL peak throughout the spin-coating process (Fig. 2j). XRD patterns of $Cs_{0.04}FA_{0.96}PbI_3$ wet films with different solvent ratios are shown in Fig. 3c. Similarly, for $Cs_{0.04}FA_{0.96}PbI_3$ wet films after annealing (Fig. 3d), all samples exhibited polycrystalline perovskite peaks at $2\theta = 13.98°$ and 28.14°, with the DMSO : NMP = 1 : 1 sample displaying the highest peak intensity. Overall, these findings demonstrate that rational regulation of intermediate-phase composition during the transition from precursor solution to wet film is crucial for obtaining high-quality, high-crystallinity perovskite films.

Scanning electron microscopy (SEM) and AFM characterization (Fig. 4) revealed that the 1 : 1 co-solvent produced films with large grains (1.73 μm average size, Fig. S7), smooth surfaces (RMS roughness = 32.3 nm for 1 : 1 co-solvent sample, 48 and 35.7 nm for DMSO and NMP only samples), and minimal cracks or pinholes of $FAPbI_3$ perovskite films prepared with MACl additives. As shown in Table S3, the full width at half maximum (FWHM) of the (001) diffraction peak for the perovskite films prepared with a DMSO : NMP ratio of 1 : 1 is the smallest—indicating improved crystallinity. Cross-sectional SEM images (Fig. 4n–p) further demonstrated uniform vertical growth and reduced voids in the 1 : 1 films, attributed to balanced solvent removal and nucleation control. The smaller grain size for films from NMP solvent only may result from the lower formation energy of the perovskite, which facilitates rapid nucleation and film formation without sufficient Ostwald ripening.[37] Although the DMSO : NMP = 1 : 0 sample also

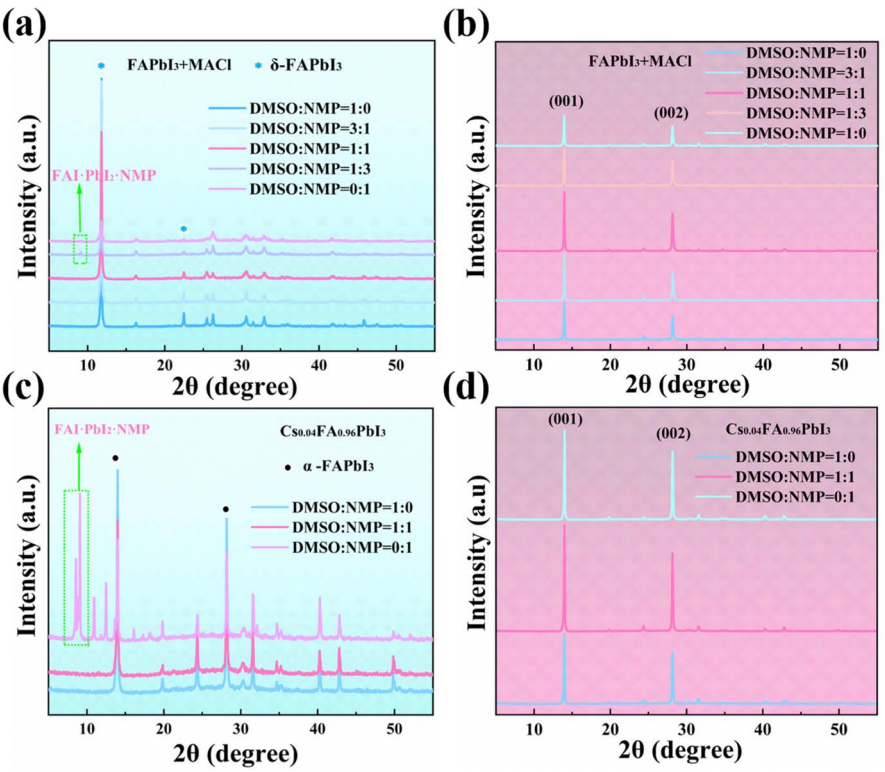

Fig. 3 The XRD patterns of (a) $FAPbI_3$ wet films with MACl additives and (c) $Cs_{0.04}FA_{0.96}PbI_3$ wet films prepared using different DMSO/NMP solvent ratios, and (b) $FAPbI_3$ films with MACl additives and (d) $Cs_{0.04}FA_{0.96}PbI_3$ films obtained after annealing.

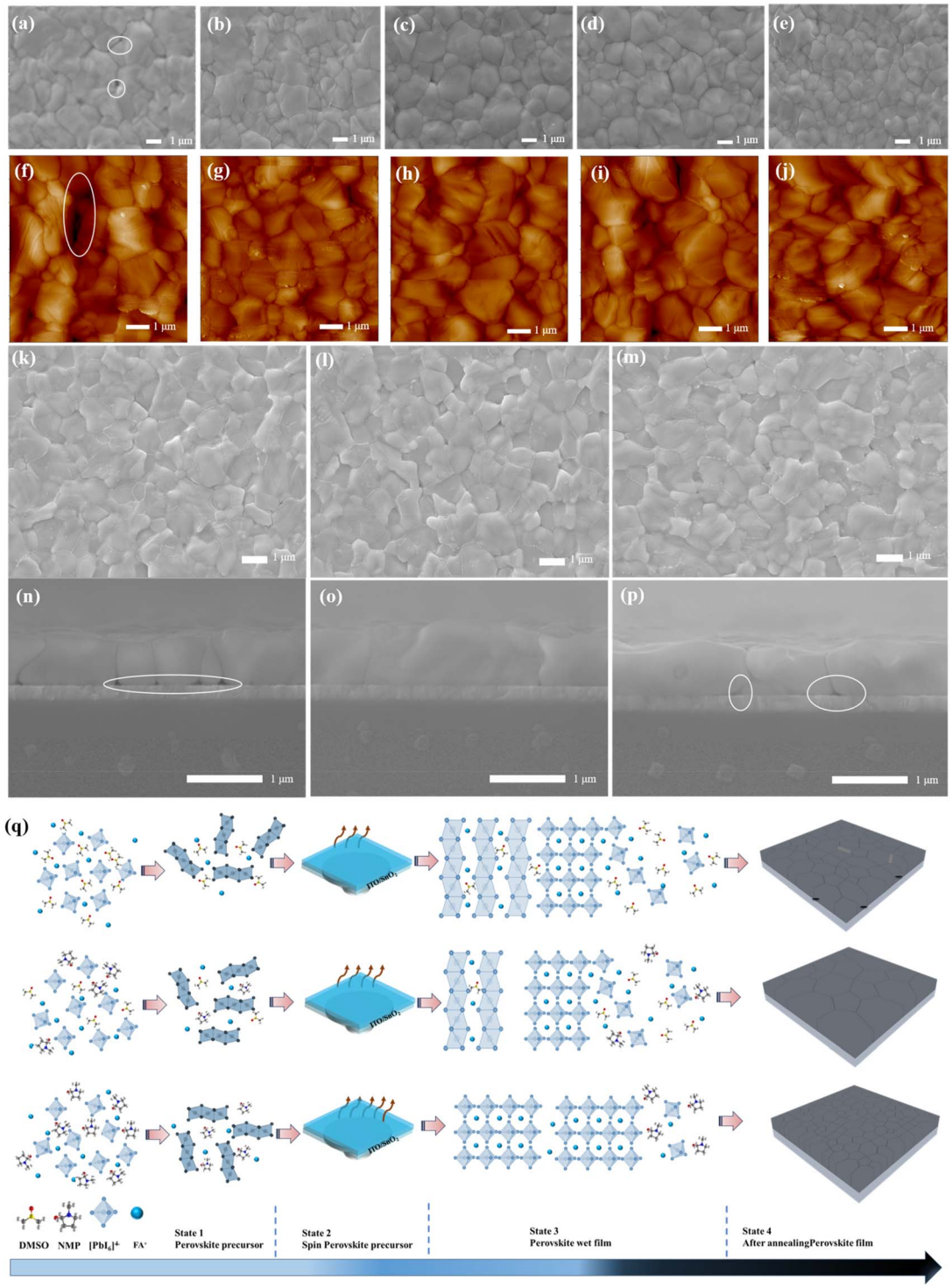

Fig. 4 SEM and AFM images of $FAPbI_3$ perovskite films prepared with MACl additives using different mixed solvents: (a and f) DMSO : NMP = 1 : 0, (b and g) DMSO : NMP = 3 : 1, (c and h) DMSO : NMP = 1 : 1, (d and i) DMSO : NMP = 1 : 3, and (e and j) DMSO : NMP = 0 : 1. The scale bar is 1 μm, and the AFM image size is 8 × 8 μm. Top-view and cross-sectional SEM images of $Cs_{0.04}FA_{0.96}PbI_3$ perovskite films prepared using different solvents: (k and n) DMSO : NMP = 1 : 0, (l and o) DMSO : NMP = 1 : 1, and (m and p) DMSO : NMP = 0 : 1. (q) Schematic illustration of the role of different solvents in the nucleation and growth of perovskite films.

displayed relatively large grains (1.55 μm, Fig. S7f), obvious cracks and pores were present (Fig. S7a). Three-dimensional AFM images (Fig. S8) further confirm the uniform and smoother surface morphology of the 1 : 1 films. Lower surface roughness can improve contact with the top hole transport layer, facilitating carrier transport and potentially contributing

to higher device current density. Similar morphology results of $Cs_{0.04}FA_{0.96}PbI_3$ films are also shown in Fig. 4 and confirmed in Fig. S9 and S7f–h. Cross-sectional SEM images of $Cs_{0.04}FA_{0.96}PbI_3$ perovskite films lead to the same conclusions as $FAPbI_3$ perovskite films prepared with MACl additives. The resulting high-quality perovskite film provides a solid foundation for fabricating high-performance devices. The crystal growth mechanism under the synergistic effect of the mixed solvent is illustrated in Fig. 4q. From the beginning, the DMSO/NMP co-solvent influences PbI_2–solvent ligand formation in the precursor solution. During spin-coating, rapid solvent removal induced by anti-solvent dripping leads to different intermediate-phase outcomes, as confirmed by XRD results (Fig. 3a and c). After thermal annealing, the intermediate phases regulated by the DMSO/NMP co-solvent yield perovskite films with better crystal quality and improved morphology. Under this co-solvent synergistic mechanism, perovskite films exhibit larger grains, fewer defects, and superior crystallinity.

Optical and electrical characterization confirmed the advantages of the co-solvent strategy. UV-vis spectra displayed similar absorption edges across all samples, with a consistent optical bandgap of 1.515 eV derived from Tauc plots (Fig. 5a and b). Steady-state photoluminescence (PL) of the 1 : 1 DMSO : NMP film on an ITO/SnO_2 substrate exhibited a noticeable blue shift and decreased intensity, indicating enhanced charge extraction and reduced shallow-level defects (Fig. 5c and S10a). The blue shift in the emission peak position is caused by a decrease in localized-state emission and a simultaneous increase in band-edge emission. Fluorescence lifetime (τ) measurements from TRPL were also performed to quantify carrier dynamics. The decay curves revealed a shorter average carrier lifetime (13.46 ns) for the 1 : 1 film compared to its 1 : 0 (43.30 ns) and 0 : 1 (19.03 ns) counterparts, indicating more efficient charge transport in the DMSO : NMP = 1 : 1 sample and then a higher short-circuit current (Fig. S9b). Space-charge-limited current (SCLC) measurements further corroborated a lower trap density of 1.48×10^{15} cm^{-3} in the 1 : 1 sample, against 2.28×10^{15} cm^{-3} and 1.73×10^{15} cm^{-3} for the 1 : 0 and 0 : 1 films, respectively (Fig. 5d–f). The trap-filled limit voltage (V_{TFL}) is determined from the intersection point corresponding to the onset of the nonlinear increase in the J–V curve beyond the ohmic region. The trap-state density (N_t) can then be calculated according to standard methods.[16]

$$N_t = \frac{2V_{TFL}\varepsilon_r\varepsilon_0}{qL^2}$$

In the equation, ε_r is the relative dielectric constant of the perovskite, ε_0 is the vacuum permittivity, q is the elementary charge, and L is the perovskite film thickness (~643 nm,

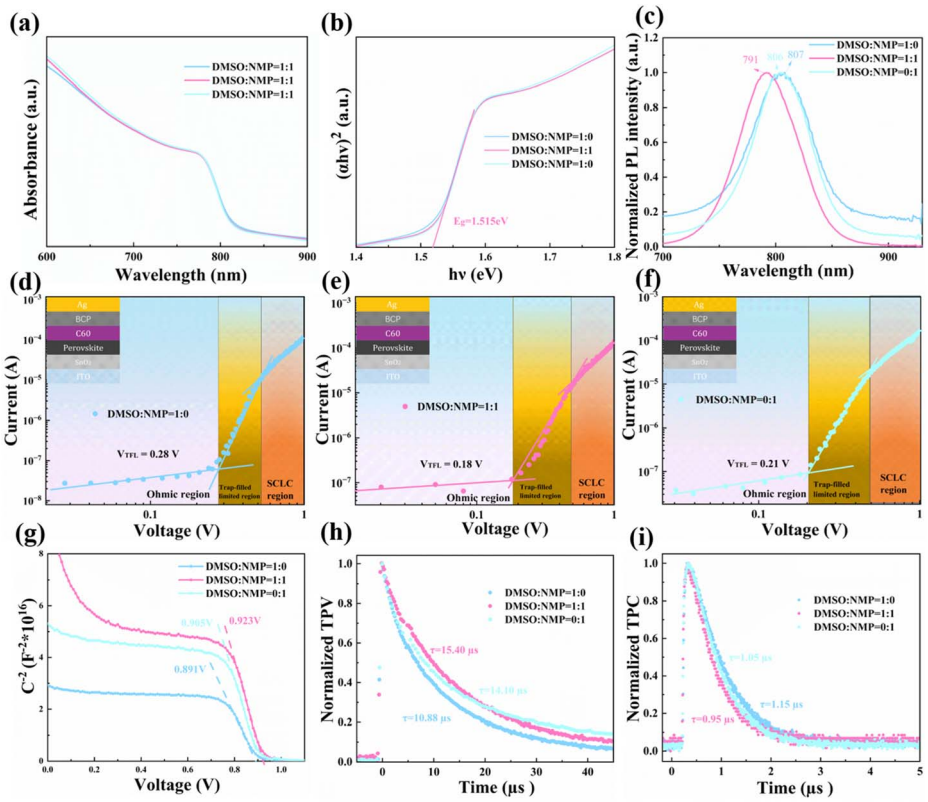

Fig. 5 (a) UV-vis absorption spectra, (b) band gaps, and (c) steady-state PL spectra of perovskite films prepared using different DMSO : NMP solvent ratios. Dark J–V curves of electron-only devices with the structure ITO/SnO_2/perovskite/C_{60}/BCP/Ag for perovskite films prepared using (d) DMSO : NMP = 1 : 0, (e) DMSO : NMP = 1 : 1, and (f) DMSO : NMP = 0 : 1 solvents. (g) Mott–Schottky plots, (h) TPV, and (i) TPC curves of PSCs based on perovskite films prepared with different DMSO : NMP solvent ratios.

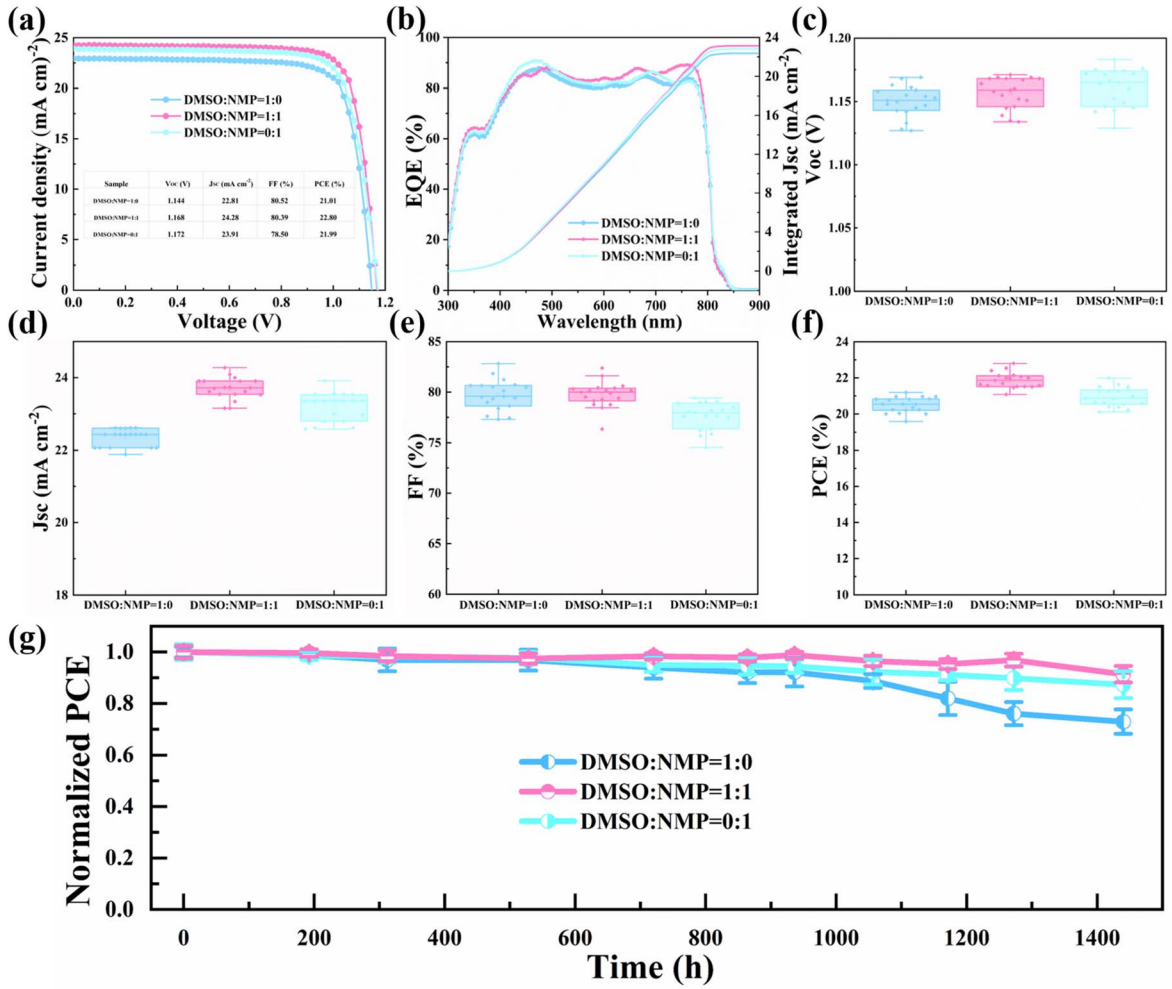

Fig. 6 (a) Comparison of J–V curves of the champion devices and their (b) EQE and corresponding integrated J_{int} curves. The stability comparison of (c) V_{OC}, (d) J_{SC}, (e) FF, and (f) PCE of un-encapsulated devices kept in the dark under humidity of 15–25% RH at room temperature. (g) Stability of PCE of the unencapsulated PSCs in ambient at ~20% RH.

Fig. S11). The reduced defect density for the DMSO : NMP = 1 : 1 sample highlights the beneficial effect of the co-solvent synergistic strategy in improving perovskite film quality. Mott–Schottky measurements indicated a higher built-in potential (0.923 V) for the 1 : 1 device, facilitating better charge injection (Fig. 5g). Transient photovoltage (TPV) and transient photocurrent (TPC) tests demonstrated a longer carrier lifetime (15.40 μs) and shorter extraction time (0.95 μs) in the 1 : 1 system, underscoring suppressed interfacial recombination and accelerated charge collection (Fig. 5h and i). Consistently, lower leakage currents were observed in 1:1-based devices (Fig. S10c), confirming superior charge transport and reduced defect-mediated losses.

Photovoltaic performance was consistently superior for devices based on the 1 : 1 co-solvent. The champion device achieved a PCE of 22.80%, with V_{oc} = 1.168 V, J_{sc} = 24.28 mA cm^{-2}, and FF = 80.39% (Fig. 6a). Statistical analysis of over 20 devices confirmed improved average performance (Fig. 6c–f). External quantum efficiency (EQE) spectra and integrated current densities aligned with J–V results (Fig. 6b); this arises from the improved perovskite film with reduced defects. The V_{oc} of devices fabricated with NMP solvent was enhanced (Fig. 6c), which was consistent with previous reports.[21] The improvement in device performance is primarily attributed to the increase in J_{sc} (Fig. 6d). The long-term stability of unencapsulated devices was evaluated under ambient air conditions (~20% relative humidity, 25 ± 5 °C). Stability tests showed that the 1 : 1-based devices retained 91% of their initial PCE after 1440 h in ambient air, outperforming their DMSO-only counterpart (73% retention) (Fig. 6g). The improved device stability is primarily attributed to the enhanced quality of the perovskite films, which effectively mitigates degradation associated with defects and moisture penetration.

3. Conclusions

In summary, this study demonstrates a synergistic DMSO/NMP co-solvent strategy for fabricating high-quality, phase-pure α-$FAPbI_3$ perovskite films. By combining ESP calculations, FTIR, *in situ* PL, and XRD, we revealed how competitive solvent

coordination regulates intermediate phase composition and crystallization kinetics. *In situ* PL monitoring during spin-coating provided insights into the evolution of the wet film, while XRD measurements clarified the composition of intermediate phases. The optimized 1 : 1 DMSO/NMP co-solvent facilitates the formation of multinuclear precursor complexes, suppresses deleterious phases, and promotes uniform film morphology with low defect density. Carrier dynamics measurements confirmed enhanced charge extraction and transport, and devices fabricated using this strategy achieved a high power conversion efficiency of 22.80% and improved operational stability, higher than their counterparts fabricated using a single solvent. Overall, this work provides mechanistic insights into co solvent engineering and offers practical guidance for solvent selection in high performance perovskite optoelectronics.

Author contributions

Q. S. conceived the idea and supervised the project. Z. J. fabricated the devices and carried out the *J–V* and EQE measurements. X. H. carried out *in situ* PL measurements. C. X. carried out the literature survey. H. Z. carried out the SEM measurement. J. Y. carried out the XRD measurement. Q. S., J. Y., and Z. J. wrote the manuscript, and all authors reviewed it.

Conflicts of interest

There are no conflicts to declare.

Data availability

The data that support the findings of this study are available from the corresponding authors upon reasonable request.

Supplementary information (SI): experimental section, Fig. S1–S11, and Tables S1–S3. See DOI: https://doi.org/10.1039/d6sc00647g.

Acknowledgements

The authors acknowledge financial support from the National Natural Foundation of China (Grant No. 12074321 and 12264060), Southwest University postgraduate research innovation project (SWUB25049), and Guizhou Province Scientific and Technological Innovation Talent Team Construction Project (QKHRCCXTD[2025]040). Part of the characterization studies was supported by Dr Zhao Yanan from the Analytical Testing Center of Southwest University.

References

1 National Renewable Energy Laboratory, *Best research-cell efficiency chart*, NREL, 2025, https://www.nrel.gov/pv/cell-efficiency.html.
2 A. Al-Ashouri, E. Köhnen, B. Li, A. Magomedov, H. Hempel, P. Caprioglio, J. A. Márquez, A. B. Morales Vilches, E. Kasparavicius and J. A. Smith, *Science*, 2020, **370**, 1300–1309.
3 R. Lin, J. Xu, M. Wei, Y. Wang, Z. Qin, Z. Liu, J. Wu, K. Xiao, B. Chen and S. M. Park, *Nature*, 2022, **603**, 73–78.
4 J. Lv, L. Le, S. Yao, Z. Huang and Y. Chen, *Chem. Sci.*, 2025, **16**, 18559–18598.
5 H. Min, M. Kim, S.-U. Lee, H. Kim, G. Kim, K. Choi, J. H. Lee and S. Seok, *Science*, 2019, **366**, 749–753.
6 J. Park, J. Kim, H.-S. Yun, M. J. Paik, E. Noh, H. J. Mun, M. G. Kim, T. J. Shin and S. Seok, *Nature*, 2023, **616**, 724–730.
7 H. Min, D. Y. Lee, J. Kim, G. Kim, K. S. Lee, J. Kim, M. J. Paik, Y. K. Kim, K. S. Kim, M. G. Kim, T. J. Shin and S. Seok, *Nature*, 2021, **598**, 444–450.
8 J. J. Yoo, G. Seo, M. R. Chua, T. G. Park, Y. Lu, F. Rotermund, Y.-K. Kim, C. S. Moon, N. J. Jeon, J.-P. Correa-Baena, V. Bulović, S. S. Shin, M. G. Bawendi and J. Seo, *Nature*, 2021, **590**, 587–593.
9 O. J. Weber, D. Ghosh, S. Gaines, P. F. Henry, A. B. Walker, M. S. Islam and M. T. Weller, *Chem. Mater.*, 2018, **30**(11), 3768–3778.
10 T. Bu, J. Li, H. Li, C. Tian, J. Su, G. Tong, L. K. Ono, C. Wang, Z. Lin, N. Chai, X.-L. Zhang, J. Chang, J. Lu, J. Zhong, W. Huang, Y. Qi, Y.-B. Cheng and F. Huang, *Science*, 2021, **372**, 1327–1332.
11 M. Kim, G.-H. Kim, T. K. Lee, I. W. Choi, H. W. Choi, Y. Jo, Y. J. Yoon, J. W. Kim, J. Lee, D. Huh, H. Lee, S. K. Kwak, J. Y. Kim and D. S. Kim, *Joule*, 2019, **3**(9), 2179–2192.
12 M. Wang, L. Li, J. Wang, H. Huang, P. Cui, Z. Lan, S. Qu, Y. Suo and M. Li, *Chem. Eng. J.*, 2025, **505**, 159056.
13 M. N. Lintangpradipto, H. Zhu, B. Shao, W. J. Mir, L. Gutiérrez-Arzaluz, B. Turedi, M. Abulikemu, O. F. Mohammed and O. M. Bakr, *ACS Energy Lett.*, 2023, **8**(11), 4915–4922.
14 C. Yang, C. Chen, T. Bian, C. Xu, X. Che, D. Li, K. Liang, X. Dong, J. Yin, G. Li and Y. Zhu, *ACS Nano*, 2025, **19**(9), 9225–9231.
15 H. Xu, Q. Zhong, Y. Ji, Q. Li, H. Yan, Y. Chen, R. Zhu and L. Zhao, *J. Energy Chem.*, 2025, **106**, 133–141.
16 Z. Z. Jiang, F. Li, H. Yan, R. K. Rathes, L. Chen, P. Li and Q. L. Song, *Green Chem.*, 2024, **26**, 5460–5470.
17 X. Wang, J. Wu, G. Zhang, R. Zhang, M. An, X. He, X. Huang, J. Gao, H. Du, Y. Wang, D. Wei, D. Chen, Y. Wang and W. Huang, *Chem. Sci.*, 2025, **16**, 23077–23087.
18 J. Wang, B. Jiao, R. Tian, K. Sun, Y. Meng, Y. Bai, X. Lu, B. Han, M. Yang, Y. Wang, S. Zhou, H. Pan, Z. Song, C. Xiao, C. Liu and Z. Ge, *Nat. Commun.*, 2025, **16**, 4148.
19 Y. Zhong, Y. Gong, H. Zhu, J. Yan, X. Zhao, J. Zhou, H. Du, L. Li, Q. Song and C. Gao, *ACS Photonics*, 2025, **12**(11), 6325–6334.
20 J.-W. Lee, Z. Dai, C. Lee, H. M. Lee, T.-H. Han, N. D. Marco, O. Lin, C. S. Choi, B. Dunn, J. Koh, D. D. Carlo, J. H. Ko, H. D. Maynard and Y. Yang, *J. Am. Chem. Soc.*, 2018, **140**(20), 6317–6324.
21 X. Huang, G. Deng, S. Zhan, F. Cao, F. Cheng, J. Yin, J. Li, B. Wu and N. Zheng, *ACS Cent. Sci.*, 2022, **8**(7), 1008–1016.
22 H. Zhu, Y. Zhong, J. You, Z. Jiang, X. He, C. Xu, Z. Dai, G. Xu and Q. L. Song, *Small*, 2025, **21**(17), 2412717.

23 X. Huang, F. Cheng, B. Wu and N. Zheng, *J. Phys. Chem. Lett.*, 2022, **13**(7), 1765–1776.
24 Z. Huang, Y. Bai, X. Huang, J. Li, Y. Wu, Y. Chen, K. Li, X. Niu, N. Li, G. Liu, Y. Zhang, H. Zai, Q. Chen, T. Lei, L. Wang and H. Zhou, *Nature*, 2023, **623**, 531–537.
25 N. Sun, S. Fu, Y. Li, L. Chen, J. Chung, M. M. Saeed, K. Dolia, A. Rahimi, C. Li, Z. Song and Y. Yan, *Adv. Funct. Mater.*, 2024, **34**, 2309894.
26 C. Li, X. Wang, E. Bi, F. Jiang, S. M. Park, Y. Li, L. Chen, Z. Wang, L. Zeng, H. Chen, Y. Liu, C. R. Grice, A. Abudulimu, J. Chung, Y. Xian, T. Zhu, H. Lai, B. Chen, R. J. Ellingson, F. Fu, D. S. Ginger, Z. Song, E. H. Sargent and Y. Yan, *Science*, 2023, **379**, 690–694.
27 Z. Wan, B. Ding, J. Su, Z. Su, Z. Li, C. Jia, Z. Jiang, Q. Qin, M. Zhang, J. Shi, H. Wu, C. Zhi, F. Wang, C. Li, L. Du, C. Zhang, Y. Ding, C. Li, X. Gao, C. Xiao, J. Chang, M. K. Nazeeruddin and Z. Li, *Energy Environ. Sci.*, 2024, **17**, 6302–6313.
28 T. Wu, J. Wu, Y. Tu, X. He, Z. Lan, M. Huang and J. Lin, *J. Power Sources*, 2017, **365**, 1–6.
29 Y.-H. Seo, E.-C. Kim, S.-P. Cho, S.-S. Kim and S.-I. Na, *Appl. Mater. Today*, 2017, **9**, 598–604.
30 Y. Li, H. Fan, F. Xu, T. Wang, C. Shan, W. Li, X. Gu, X. Lai, D. Luo, Z. Sun, M. Zhao, X. Li, K. Cui, G. Li and A. K. K. Kyaw, *Sol. RRL*, 2022, **6**, 2200816.
31 A. Kulkarni, R. Sarkar, S. Akel, M. Häser, B. Klingebiel, M. Wuttig, S. Wiegand, S. Chakraborty, M. Saliba and T. Kirchartz, *Adv. Funct. Mater.*, 2023, **33**, 2305812.
32 Y. Li, X. Guan, Y. Meng, J. Chen, J. Lin, X. Chen, C.-Y. Liu, Y. Zhao, Q. Zhang, C. Tian, J. Lu and Z. Wei, *InfoMat*, 2024, **6**(5), e12537.
33 A. D. Taylor, Q. Sun, K. P. Goetz, Q. An, T. Schramm, Y. Hofstetter, M. Litterst, F. Paulus and Y. Vaynzof, *Nat. Commun.*, 2021, **12**, 1878.
34 S. Chen, X. Dai, S. Xu, H. Jiao, L. Zhao and J. Huang, *Science*, 2021, **373**, 902–907.
35 K. Mo, X. Zhu, M. Yang, Z. Xue, S. Li, M. li, Y. Yang, S. Cheng, H. Li, Q. Lin and Z. Wang, *Adv. Energy Mater.*, 2025, **15**, 2404538.
36 R. Yin, Y. Wu, Z. Huang, A. S. Vasenko, S. Xu and H. Zhou, *Adv. Funct. Mater.*, 2025, **35**, 2419184.
37 Y. Yang, J. Wu, X. Wang, Q. Guo, X. Liu, W. Sun, Y. Wei, Y. Huang, Z. Lan, M. Huang, J. Lin, H. Chen and Z. Wei, *Adv. Mater.*, 2020, **32**, 1904347.